ACES Asian Chemical Editorial Society

DOI: 10.1002/cnma.202000067

CHEMNANOMAT
Full Paper

Microporous Organic Nanoparticles Anchoring CeO_2 Materials: Reduced Toxicity and Efficient Reactive Oxygen Species-Scavenging for Regenerative Wound Healing

Dong Wook Kim[+],[a] Thai Minh Duy Le[+],[b] Sang Moon Lee,[c] Hae Jin Kim,[c] Yoon-Joo Ko,[d] Ji Hoon Jeong,[e] Thavasyappan Thambi,*[b] Doo Sung Lee,*[b] and Seung Uk Son*[a]

Abstract: This work shows that microporous organic polymer can be applied to the engineering of CeO_2-based antioxidant nanomaterials for *in vivo* regenerative wound healing. Whilst nanoparticulate CeO_2 has shown excellent redox quenching of reactive oxygen species (ROS) because it is rich in oxygen defects and Ce^{3+} species, it has a strong tendency to form aggregates because it is a kinetic intermediate of bulk materials. Anchoring of nanoparticulate CeO_2 on suitable supports can be an efficient anti-aggregation strategy. In this work, CeO_2 nanoparticles were immobilized on microporous organic nanoparticles (MONPs) to form MONP@CeO_2 nanocomposites. Compared to CeO_2 materials, the MONP@CeO_2 nanocomposites showed not only efficient ROS scavenging in *in vivo* regenerative wound healing but also reduced cytotoxicity in *in vitro* cell studies, due to the efficient distribution and dilution effect of CeO_2 nanomaterials.

Introduction

The understanding, control, and utilization of reactive oxygen species (ROS) has been a continuing research subject.[1–2] Whilst the ROS are generated naturally in bio-systems,[1] they can be manipulated and controlled artificially.[2] For example, the ROS have been generated and utilized in the oxygen-based photocatalytic decomposition of organic pollutants in water by inorganic semiconductor materials.[2]

In bio-systems, it has been known that injury of skin induces the generation of ROS in high amount.[3–4] At wound sites, the ROS are utilized in the oxidative defense against pathogens. Although the ROS play a constructive role in wound healing, usually, over-generated ROS are problematic and damage tissues. Recently, the scavenging of ROS has attracted significant attention of scientists as a strategy to help regenerative wound healing.[3] In this regard, recently, functional additives have been developed for the ROS scavenging in wound sites.[1,3,5]

Recently, CeO_2 nanomaterials have attracted special attention of scientists in bio-research field.[5] Among inorganic materials, the nanoparticulate CeO_2 has shown excellent redox quenching of ROS because it is rich in oxygen vacancy and Ce^{3+} species.[5–6] Because the oxygen vacancy and Ce^{3+} species in CeO_2 increase sharply at nanoscale and thus, the ROS scavenging performance of CeO_2 is dependent on its size and surface area,[6] the size-maintenance of nanoparticulate CeO_2 is important for efficient ROS scavenging performance.

Recently, various inorganic materials have been engineered at nanoscale.[7] Whilst unprecedented chemical and physical properties have been discovered in the nano-scaled inorganic materials, the increased surface areas, due to reduced sizes, could enhance the functional performance of nanomaterials.[7–8] Nano-scaled inorganic materials are not thermodynamically stable and have a strong tendency to form bulk materials.[9] Thus, nano-scaled inorganic materials can be regarded as kinetically controlled systems.[10] Aggregation is an inevitable phenomenon of nanomaterials, implying that the benefits of their enhanced surface areas can easily be diminished.[11] To maintain the surface-related performance of nanomaterials, there should be efficient strategies to hinder the aggregation.[12] For example, anchoring of nanomaterials on solid supports can be an option to retard their aggregation.[13] For this, suitable chemistry for solid supports is required.

Recently, various microporous organic polymers (MOPs) have been prepared.[14] The size and morphology of MOP materials have been controlled to nanoscale.[15–16] It can be expected that the MOP nanoparticles (MONPs) can serve as

[a] D. W. Kim,[+] Prof. S. U. Son
Department of Chemistry
Sungkyunkwan University
Suwon 16419 (Korea)
E-mail: sson@skku.edu

[b] T. M. D. Le,[+] Dr. T. Thambi, Prof. D. S. Lee
School of Chemical Engineering
Theranostic Macromolecules Research Center
Sungkyunkwan University
Suwon 16419 (Korea)
E-mail: thambi@skku.edu
dslee@skku.edu

[c] Dr. S. M. Lee, Dr. H. J. Kim
Korea Basic Science Institute
Daejeon 34133 (Korea)

[d] Dr. Y.-J. Ko
Laboratory of Nuclear Magnetic Resonance
National Center for Inter-University Research Facilities (NCIRF)
Seoul National University
Seoul 08826 (Korea)

[e] Prof. J. H. Jeong
School of Pharmacy
Theranostic Macromolecules Research Center
Sungkyunkwan University
Suwon 16419 (Korea)

[+] These authors contributed equally.

Supporting information for this article is available on the WWW under https://doi.org/10.1002/cnma.202000067

nanosupports for functional inorganic nanomaterials.[17] For example, the CeO_2 nanoparticles can be immobilized on MONP through the interaction of Ce species with π-electrons of MONP, hindering the aggregation of CeO_2 materials. However, as far as we are aware, the bioapplication of MOP is at an early stage.[18] Recently, our research group has reported the application of MOP to drug delivery systems for cancer therapy.[18e,f] Also, we have shown that organic polymers are helpful in the regenerative wound healing.[19] In this work, we report the synthesis of MONP@CeO_2 nanocomposites and their application to regenerative wound healing.

Results and Discussion

Figure 1 shows a synthetic scheme for MONP@CeO_2 nanocomposites. MONP nanosupports were prepared by Sonogashira coupling of tetra(4-ethynylphenyl)methane[20] with 1,4-diiodobenzene in the presence of poly(vinylpyrrolidone) (PVP).[17] Then, CeO_2 was synthesized in the presence of MONP through the decomposition of $Ce(OAc)_3$.[21] We gradually increased the amount of $Ce(OAc)_3$ from 0.079 mmol to 0.16, 0.24, and 0.32 mmol, resulting in four MONP@CeO_2 nanocomposites which were denoted as MONP@CeO_2-1, MONP@CeO_2-2, MONP@CeO_2-3, and MONP@CeO_2-4, respectively. In addition, we prepared CeO_2 nanomaterials in the absence of MONP as a control material.

As shown Figure 2a, scanning electron microscopy (SEM) of the CeO_2 materials prepared in the absence of MONP showed granular aggregates with irregular sizes in the range of 20~500 nm. Transmission electron microscopy (TEM) showed that

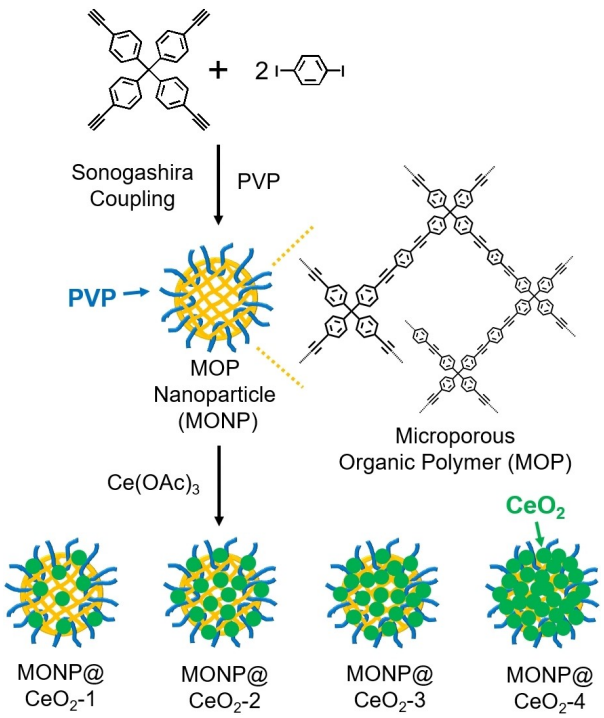

Figure 1. A synthetic scheme of MONP@CeO_2 nanocomposites.

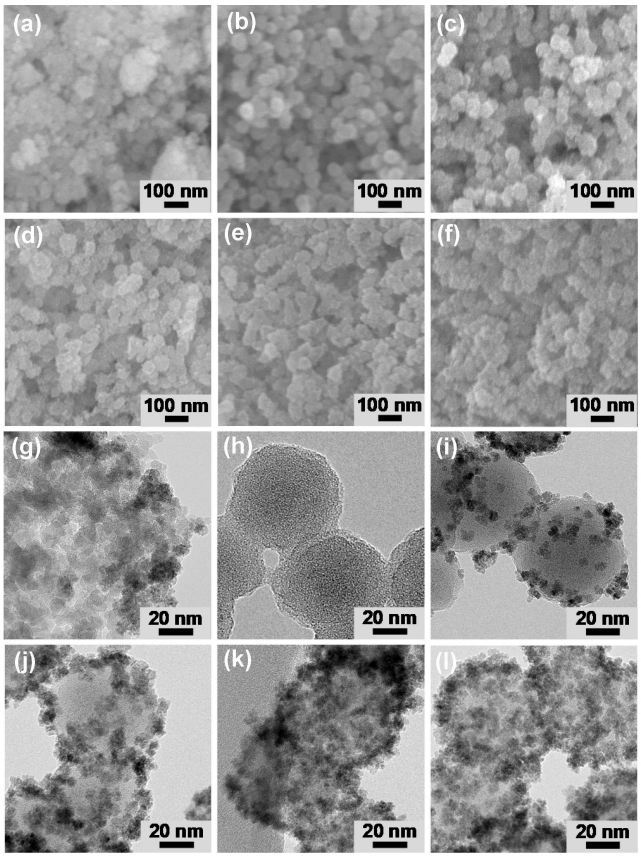

Figure 2. SEM images of (a) CeO_2, (b) MONP, (c) MONP@CeO_2-1, (d) MONP@CeO_2-2, (e) MONP@CeO_2-3, and (f) MONP@CeO_2-4. TEM images of (g) CeO_2, (h) MONP, (i) MONP@CeO_2-1, (j) MONP@CeO_2-2, (k) MONP@CeO_2-3, and (l) MONP@CeO_2-4.

the CeO_2 aggregates consist of small CeO_2 particles in the size range of 5~15 nm. (Figure 2g) SEM image of the MONP showed fairly homogeneous particles with an average size of 65 nm. (Figure 2b and S1 in the SI) TEM and high resolution (HR) TEM images showed microporosity of the MONP. (Figure 2h and S2 in the SI) SEM and TEM images of the MONP@CeO_2 showed that CeO_2 particles with sizes of 3~5 nm formed on the surface of MONP without independent CeO_2 materials. (Figures 2c–f, 2i–l, and S2 in the SI) The amount of CeO_2 nanoparticles on the MONP supports gradually increased from MONP@CeO_2-1 to MONP@CeO_2-2, MONP@CeO_2-3, and MONP@CeO_2-4. Elemental mapping analysis based on energy dispersive X-ray spectroscopy (EDS) supported the successful anchoring of CeO_2 nanoparticles on the MONPs (Figure S3 in the SI).

Powder X-ray diffraction (PXRD) studies showed that the MONP has amorphous characteristic[22] and that the nanoparticles on the MONP are CeO_2 (JCPDS # 81-0792) with (111), (200), (220), (311), (222), (440), and (331) diffraction peaks at 2θ of 28.6, 33.2, 47.4, 56.2, 59.0, 69.4, and 76.6°, respectively. (Figure 3a) X-ray photoelectron spectroscopy (XPS) of the CeO_2 and MONP@CeO_2 nanocomposites showed a mixed state of Ce^{3+} (3d orbital peaks at 880.4, 884.9, 898.8, and 903.4 eV) and Ce^{4+} species (3d orbital peaks at 882.1, 888.7, 898.1, 900.5,

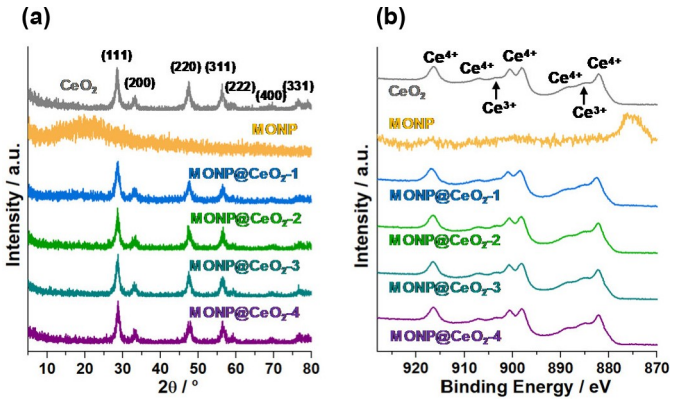

Figure 3. (a) PXRD patterns and (b) XPS spectra of CeO_2, MONP, and MONP@CeO_2 nanocomposites.

907.1, and 916.4 eV), which is a unique observation in the nanosized CeO_2 materials with oxygen vacancies[7] (Figure 3b).

By analysis of N_2 sorption isotherm curves, surface areas of the MONP and CeO_2 were measured to be 548 and 72 m^2/g with pore volumes of 0.66 and 0.07 cm^2/g, respectively. (Figure 4a) Surface areas of MONP@CeO_2-1, MONP@CeO_2-2, MONP@CeO_2-3, and MONP@CeO_2-4 were measured to be 425, 315, 279, and 249 m^2/g with pore volumes of 0.55, 0.51, 0.45, and 0.35 cm^3/g, respectively (Figure 4b and Table 1).

In infrared (IR) absorption spectrum, the MONP showed main peaks at 1683, 1501, and 820 cm^{-1}, corresponding to C=O (PVP), aromatic C=C, and aromatic C–H vibrations, respectively. (Figure 4c) In comparison, as the amount of CeO_2 in MONP@CeO_2 increased, the intensities of IR peak at 507 cm^{-1} (Ce–O vibration) increased in addition to the IR peaks of 1427, and 1548 cm^{-1}, corresponding to the vibrations of surface oxygen species.[23] Thermogravimetric analysis (TGA) showed that the MONP and MONP@CeO_2 nanocomposites are stable up to 325 °C. (Figure 4d) Solid state ^{13}C nuclear magnetic resonance (NMR) spectroscopy of MONP showed ^{13}C peaks at 121 ~ 145, 90, and 63 ppm, corresponding to aromatic groups, internal alkynes, and benzyl carbon, respectively. (Figure 4e) In addition, ^{13}C peaks were observed at 17 ~ 49 and 174 ppm, corresponding to aliphatic and carbonyl groups of PVP, respectively, supporting that the MONP with entrapped PVPs was formed by Sonogashira coupling of building blocks. The ^{13}C NMR spectrum of MONP@CeO_2-2 was the same with that of MONP, indicating the retention of chemical structure (Figure S4 in the SI).

According to elemental analysis, the contents of CeO_2 in the MONP@CeO_2-1, MONP@CeO_2-2, MONP@CeO_2-3, and MONP@CeO_2-4 were measured to be 18.7, 33.5, 46.3, and 54.9 wt%, respectively. (Table 1) The contents of Ce in the MONP@CeO_2-1, MONP@CeO_2-2, MONP@CeO_2-3, and MONP@CeO_2-4 were measured to be 1.45, 2.19, 2.84, and 2.86 mmol/g, respectively, by inductively coupled plasma (ICP) analysis.

Whilst zeta potentials of the CeO_2 and MONP were measured to be −14.5 and −14.9 mV in water, respectively, those of MONP@CeO_2 composites were shifted to more negative values (−31.2 ~ −32.5 mV), due to the efficient distribution of CeO_2 on the MONP. (Table 1 and Figure S5 in the SI) The existence of PVP made the MONP water-compatible.[17] Whilst hydrodynamic average diameters of the CeO_2 and MONP were measured to be 255 and 83 nm, respectively, by dynamic light scattering (DLS) studies, those of MONP@CeO_2 composites increased gradually from 104 nm (MONP@CeO_2-1) to 126 (MONP@CeO_2-2), 134 (MONP@CeO_2-3), and 135 nm (MONP@CeO_2-4) with an increase of CeO_2 amount. (Table 1 and

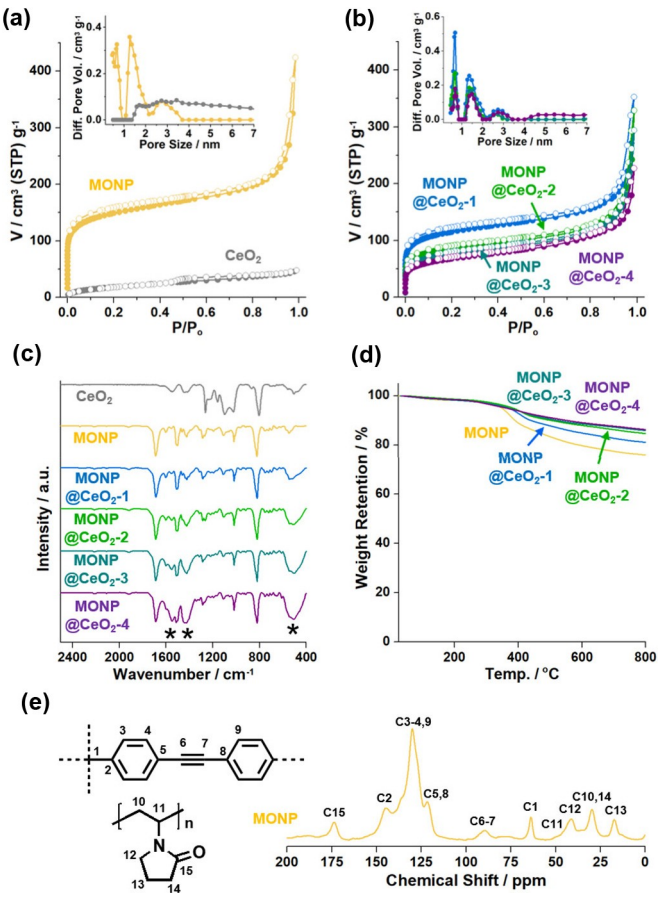

Figure 4. (a–b) N_2 adsorption-desorption isotherm curves at 77 K and pore size distribution diagrams (based on the DFT method), (c) IR spectra, and (d) TGA curves of CeO_2, MONP, and MONP@CeO_2 composites. (e) Solid state ^{13}C NMR spectrum of MONP.

Table 1. Chemical and physical properties of CeO_2, MONP, and MONP@CeO_2 composites.

Entry	Materials	CeO_2[a] [wt%]	S_{BET}[b] [m^2/g]	V_{tot}[c] [cm^3/g]	Z[d] [mV]	D[e] [nm]
1	CeO_2	100	72	0.07	−14.5	255
2	MONP	0	548	0.66	−14.9	83
3	MONP@CeO_2-1	18.7	425	0.55	−31.9	104
4	MONP@CeO_2-2	33.5	315	0.51	−32.5	126
5	MONP@CeO_2-3	46.3	279	0.45	−31.8	134
6	MONP@CeO_2-4	54.9	249	0.35	−31.2	135

[a] Contents of CeO_2 based on elemental analysis. [b] Surface areas based on the Brunauer-Emmett-Teller theory. [c] Total pore volume. [d] Zeta potential in water. [e] Hydrodynamic diameter measured by DLS studies in water.

Figure 5a) It is noteworthy that the elimination process of nanomaterials from body depends on their sizes.[24–25] It is well known that the nanomaterials with sizes greater than 10 nm extravasate into liver through liver sinusoidal fenestrations and thereafter, hepatocytes in the liver eliminate foreign substances by endocytosis, followed by enzymatic breakdown and excretion into the bile.[24–25]

To study ROS scavenging function of the MONP@CeO_2 composites, we tested their catalytic performance in the H_2O_2 decomposition to water and O_2.[26] (Figure 5b) It is noteworthy that H_2O_2 is one of main ROS generated in wound sites.[1–5] The control CeO_2 material showed a relatively poor catalytic performance, due to its aggregated nature. (Figure 5b) Whilst the MONP@CeO_2-1 showed good catalytic performance over 3 h, its catalytic durability decreased after 3 h, implying that the proper aggregation of CeO_2 nanoparticles enhances the stability of systems. (Figure 5b) After 8 h, the catalytic efficiencies of CeO_2 in the materials were in the order of MONP@CeO_2-2 > MONP@CeO_2-3 > MONP@CeO_2-4 > MONP@CeO_2-1 > CeO_2, indicating that the MONP serves as a good nanosupport for the efficient distribution of CeO_2 materials. In a control test, the MONP showed negligible catalytic activity in the H_2O_2 decomposition (Figure S6 in the SI).

In vitro cytotoxicity of materials toward human 293T and mouse NIH 3T3 cells was investigated by MTT assay. (Figures 5c–d and S7–8 in the SI). whilst the CeO_2 showed potential cytotoxicity (cell viability < 90%) in the concentration of > 10 μg/mL, cytotoxicity was significantly reduced in the MONP@CeO_2 composites with cell viabilities > 90% even at 1000 μg/mL, due to the dilution effect of the CeO_2 in the MONP materials. (Figures 5c–d) In a control test, the MONP showed cell viability of 86% at 1000 μg/mL (Figure S7 in the SI).

Next, we studied the effects of CeO_2, MONP, and MONP@CeO_2 materials in *in vivo* regenerative wound healing of Spraque-Dawley (SD) rats (n = 3). The same amount of CeO_2, MONP, and MONP@CeO_2 nanocomposites were added to linear cuts (1 cm length and 1 ~ 1.2 mm depth, penetrating a subcutaneous tissue layer[27] of skin) of SD rats. (Figure 6a) The closure kinetics of cuts was investigated and quantificated (n = 3) by measuring the changes of wounds. Figures 6b–7 summarize the results. Whilst all MONP@CeO_2 nanocomposites showed better performance than a blank control system, CeO_2, and MONP, the MONP@CeO_2-2 showed the best performance. In addition, as time passed, the beneficial effect of CeO_2 distribution on the MONP became more significant (Figure 6b).

After 7 days, whilst a blank control system showed wound retention of 43 ± 3%, the control materials of CeO_2 and MONP showed wound retention of 26 ± 3 and 27 ± 2%, respectively. (Figure 7a) The enhanced wound healing by CeO_2 and MONP, compared to the blank control system, is attributable to the ROS scavenging function of CeO_2 and the nanobridging effect[19] of nanoadditives in wounds, as illustrated in Figure 6a.

In cases of the MONP@CeO_2 nanocomposites, after 7 days, whilst the MONP@CeO_2-1, MONP@CeO_2-3, and MONP@CeO_2-4 showed much enhanced wound healing with wound retention of 18 ± 2, 14 ± 2 and 22 ± 2%, respectively, the MONP@CeO_2-2 showed nearly complete wound healing with wound retention of 0 ± 1%. (Figure 7b) The observed results are attributable to the optimal distribution of CeO_2 by MONP in the MONP@CeO_2-2 nanocomposite, inducing the efficient redox quenching of ROS and the reduced cytotoxicity due to the dilution effect of CeO_2. In addition, the enhanced negative zeta potentials of MONP@CeO_2 nanocomposites, compared to CeO_2, can be beneficial in maintaining their ROS scavenging functions. We suggest that the contamination of nanocomposites by blood proteins such as albumin with negative zeta potentials can be suppressed through charge-charge repulsion.[28]

After regenerative wound healing for 7 days, the resulant skin tissues were investigated by histological analysis. As shown in Figure 7c, the H&E and Masson's trichrome-stained skin tissues indicate complete re-epithelialization and recovery of collagen structures after wound healing by the MONP@CeO_2-2 for 7 days.

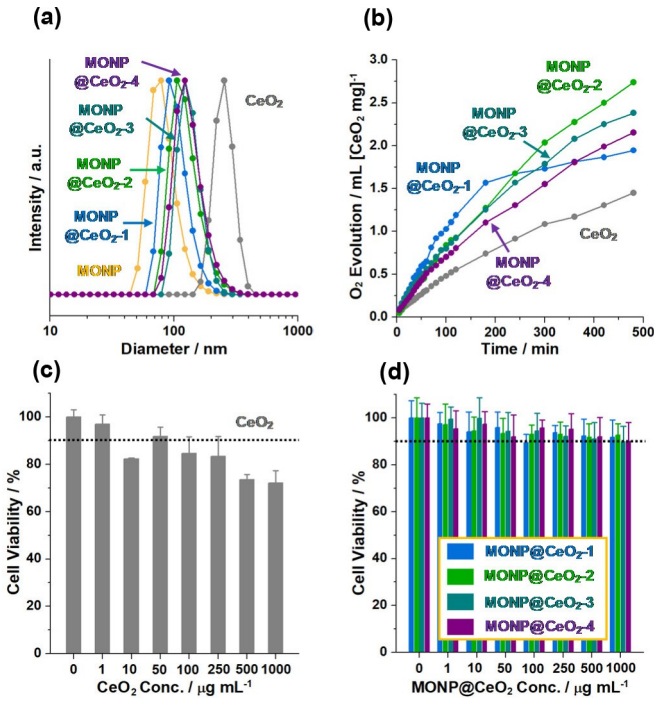

Figure 5. (a) Hydrodynamic diameters of CeO_2, MONP, and MONP@CeO_2 nanocomposites in water. (b) H_2O_2 decomposition to water and O_2 catalyzed by CeO_2 and MONP@CeO_2 nanocomposites. (refer to Figure S5 in the SI for the catalytic acitivity of MONP for the H_2O_2 decomposition). *In vitro* cytotoxcity of (c) CeO_2 and (d) MONP@CeO_2 nanocomposites measured by MTT assay using human embryonic kidney 293T cells (refer to Figure S6 in the SI for MTT assay of MONP).

Conclusion

This work shows that MOP nanoparticles can serve as nanosupports of functional inorganic materials for bioapplications. The ROS scavenging function of CeO_2 materials could be enhanced through the distribution of CeO_2 materials on the MONP. In addition to the anti-aggregation benefit, the MONP@CeO_2 nanocomposites showed reduced cytotoxicity, compared to CeO_2, due to the dilution effect. The MONP@CeO_2-2

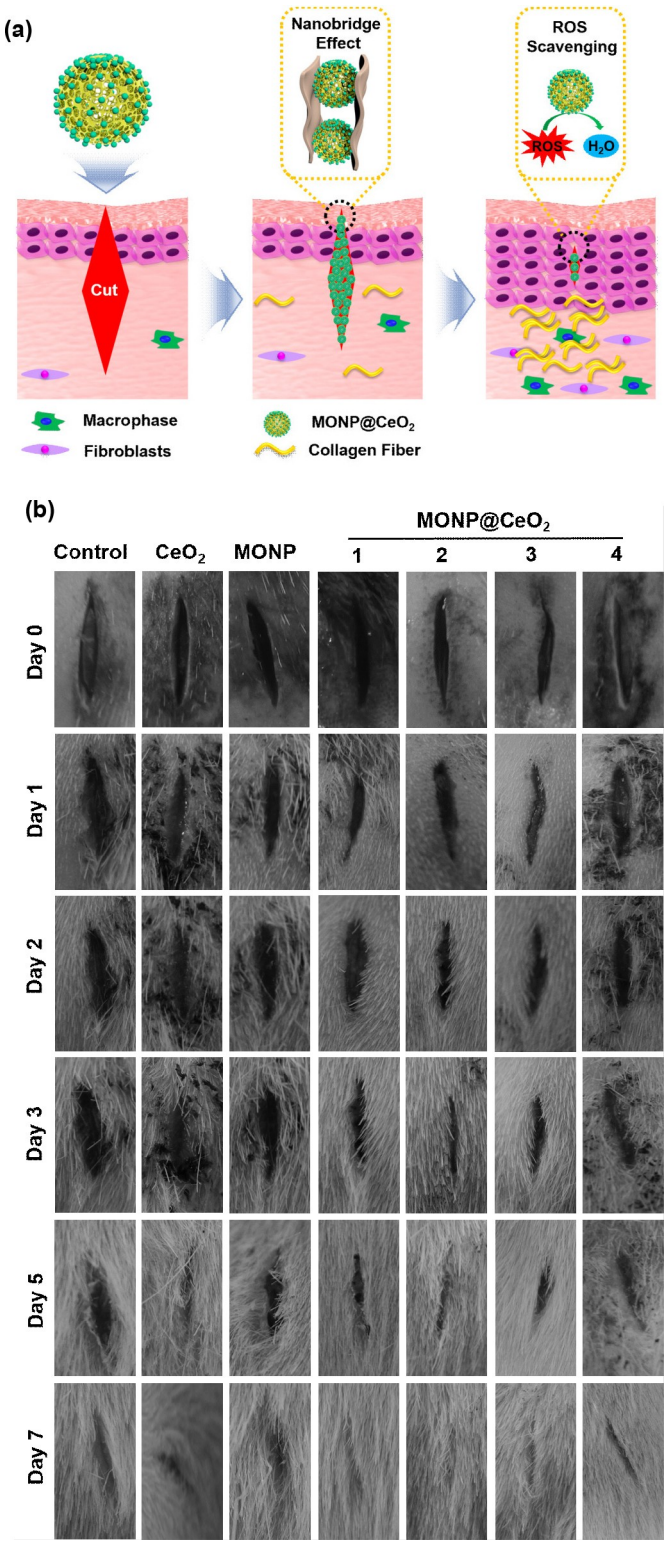

Figure 6. (a) A schematic illustration of the MONP@CeO_2-assisted regenerative wound healing process. (b) Photographs of the *in vivo* regenerative wound healing processes of Spraque-Dawley rats with linear cuts (1 cm length and 1 ~ 1.2 mm depth) over 7 days by a blank control system, CeO_2, MONP, and MONP@CeO_2 nanocomposites.

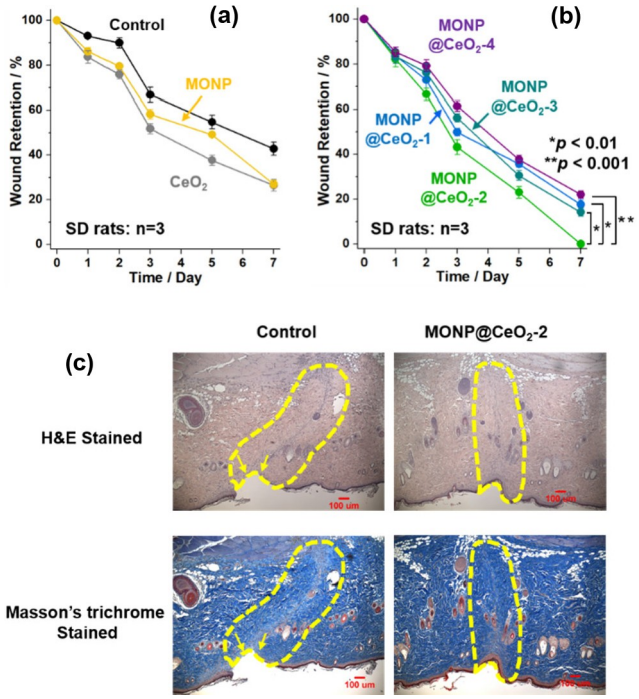

Figure 7. (a–b) Quantificated *in vivo* wound closure kinetics of CeO_2, MONP, and MONP@CeO_2 nanocomposites (SD rats: n = 3). (c) H&E and Masson's trichrome stained skin tissues (SD rats) after regenerative wound healing by a blank control system and MONP@CeO_2-2 for 7 days.

with an optimal composition showed the best performance. We believe that the MOP nanoparticles with high surface areas and microporosity can be applied to the engineering of more various nanocomposites for bioapplications.

Experimental Section

Generation information

SEM and TEM images were obtained by a FE-SEM (JSM6700F) and a JEOL 2100F, respectively. PXRD patterns were obtained by a Rigaku MAX-2200. N_2 adsorption-desorption isotherm curves were obtained by a Micromeritics ASAP2020. Pore size distribution was analyzed by the DFT method. IR absorption spectra were obtained by a Bruker VERTEX 70 FT-IR spectrometer. TGA curves were obtained by a Seiko Exstar 7300. Solid state ^{13}C NMR spectrum was obtained at CP/TOSS mode by a 500 MHz Bruker ADVANCE II NMR spectrometer at the NCIRF of Seoul National University. Elemental analysis was performed by a CE EA1110 analyzer. ICP analysis was conducted using an OPTIMA 8300. Zeta potentials and hydrodynamic diameters were measured by a Zetasizer ZS90 (Malvern). XPS spectra were obtained by a Thermo VG spectrometer.

Synthesis of MONP, CeO_2, and MONP@CeO_2 nanocomposites

MONP was prepared by the synthetic procedures modified from the literature.[17] In this study, for the preparation of MONP, $(PPh_3)_2PdCl_2$ (21 mg, 30 μmol), CuI (5.8 mg, 30 μmol), and triethylamine (25 mL) were added to a 100 mL Schlenk flask under argon. Polyvinylpyrrolidone (PVP, Mw: 40000, 1.55 g) dissolved in ethanol

(50 mL) was added to the reaction mixture. After the reaction mixture was sonicated for 40 min at room temperature, tetra(4-ethynylphenyl)methane[20] (0.125 g, 0.300 mmol) and 1,4-diiodobenzene (0.198 g, 0.600 mmol) were added. The reaction mixture was stirred at 100 °C for 1 day. After being cooled to room temperature, solid was separated by centrifugation, washed with methanol (40 mL) thrice and methylene chloride (40 mL) thrice, and dried under vacuum.

For the preparation of MONP@CeO_2-2, MONP (25 mg) was added to ethanol (5 mL) in a 25 mL Schlenk flask. The reaction mixture was sonicated for 15 min at room temperature. Cerium acetate hydrate (50 mg, 0.16 mmol) was dissolved in distilled water (20 mL) through sonication in a vial. After the cerium acetate aqueous solution was added, the reaction mixture was stirred at 80 °C for 1 day. The solid was separated by centrifugation, washed with water (40 mL) thrice and ethanol (40 mL) thrice, and dried under vacuum. For the preparation of MONP@CeO_2-1, MONP@CeO_2-3, and MONP@CeO_2-4, 25 mg (0.079 mmol), 75 mg (0.24 mmol), and 100 mg (0.32 mmol) of cerium acetate hydrate were used. The other synthetic procedures were the same as those applied for MONP@CeO_2-1. For the preparation of a control CeO_2 nanomaterial, the same synthetic procedures as those applied for MONP@CeO_2-4 were applied without using MONP.

Experimental procedures for the catalytic decomposition of H_2O_2

For the catalytic decomposition of H_2O_2 by CeO_2 and MONP@CeO_2 nanocomposites, the experimental procedures modified from the literature[29] were applied. A separatory funnel with water was connected to one neck of a 100 mL two-neck Schlenk flask using a silicon tube and a glass joint. A gas bubbler was connected to a cork of the 100 mL two-neck Schlenk flask using a silicon tube. After H_2O_2 solution (0.20 M, 25 mL) was added to catalytic material (20 mg) in the 100 mL two-neck Schlenk flask at 25 °C (water bath temperature), the other neck was closed using a rubber septum. The reaction mixture was stirred at 300 rpm. As the oxygen gas was generated, the meniscus of the gas bubbler went down. To maintain the original height of the meniscus, the cork of the separatory funnel was opened. The volume of drained water at the given reaction time was measured by a messcylinder. Considering the vapor pressure of water at 25 °C, the volume of the generated oxygen gas was calculated.

In vitro cytoxicity

The *In vitro* cytotoxicity of MONP, CeO_2, and MONP@CeO_2 nanocomposites was examined using human embryonic kidney 293T and mouse NIH 3T3 cells *via* MTT assay. The cells were cultured in RPMI medium supplemented with 10% FBS and 1% pencillin-streptomycin in a humidifed atmosphere. Thereafter, the cells were trypsinized, seeded in a 96-well plate at a density of 1×10^4 cells/well and allowed to grow for 24 h. The cells were then washed with PBS and incubated with various concentrations of MONP, CeO_2, and MONP@CeO_2 nanocomposites for 24 h. The cells incubated with medium alone served as a control system. Then, the cells were washed twice with PBS to remove remaining materials and incubated with fresh medium containing MTT solution (20 μL, 5 mg/mL) for 4 h. The culture medium was then removed and the purple crystals (formazan) were dissolved uisng DMSO to examine the viability. The absorbance of each well (at 490 nm) was measured on a microplate reader (Multiskan Go, Winooski, VT, USA) to calculate the cell viability.

Wound healing

For our wound healing studies, Sprague-Dawley rats (SD rats, 200–220 g) were purchased from the Korea Research Institute of Bioscience and Biotechnology (KRIBB, Daejeon, Korea). Live animal experiments were performed in accordance with the institutional guidelines of Sungkyunkwan University. The Sungkyunkwan University institutional committees approved all of our animal experiments.

For the wound healing studies, the SD rats were anesthetized with pentobarbital and then, linear open wounds (1 cm length and 1 ~ 1.2 mm depth) were created. The SD rats were randomly divided into seven different groups (n = 3); (i) a blank control system (without any treatment), (ii) CeO_2 (5 mg/ml), (iii) MONP (5 mg/ml), (iv) MONP@CeO_2-1 (5 mg/ml), (v) MONP@CeO_2-2 (5 mg/ml), (vi) MONP@CeO_2-3 (5 mg/ml), (vii) MONP@CeO_2-4 (5 mg/ml). The hyaluronic acid (HA, 10 mg/ml) was added to the CeO_2, MONP, MONP@CeO_2 nanocomposite solutions. The materials were well dispersed in aqueous solution and stayed on the wound bed. After the wound creation, no treatments were provided for the blank control group. For other cases, the CeO_2, MONP, and nanocomposite solutions (150 μL) were transferred to small syringe (1 mL, 26G) and added to the wound area. The wound healing was monitored at 0, 1, 2, 3, 5, and 7 days and photographed to measure the extent of wound healing. Statistical analysis between the control and other tests was performed by one-way analysis of variance (ANOVA). Values indicate a mean standard deviation.

After 7 days, the rats were euthanized and skins were harvested. For histological analysis, the collected skin tissues were fixed using 10% formalin and embedded in paraffin. Then, skin tissues were sliced (~4 μm thickness) and used for hematoxylin & eosin (H&E) and Masson's trichrome (MT) staining. The stained slides were visualized using the microscope to examine the order of wound healing.

Acknowledgements

This work was supported by the National Research Foundation of Korea (NRF) grant (No. 2020R1A2C200431011, NRF-2016R1A6A3A11931661, NRF-2017R1D1A1B03028061) funded by the Korea government (MSIT).

Conflict of Interest

The authors declare no conflict of interest.

Keywords: Microporous organic polymer · CeO_2 · Nanocomposites · Reactive oxygen species · Regenerative wound healing

[1] Y. Yao, H. Zhang, Z. Wang, J. Ding, S. Wang, B. Huang, S. Ke, C. Gao, *J. Mater. Chem. B* **2019**, *7*, 5019–5037.
[2] Y. Nosaka, A. Y. Nosaka, *Chem. Rev.* **2017**, *117*, 11302–11336.
[3] M. Schäfer, S. Werner, *Pharmacol. Res.* **2008**, *58*, 165–171.
[4] P. Niethammer, C. Grabher, A. T. Look, T. J. Mitchison, *Nature* **2009**, *459*, 996–1000.
[5] a) C. Walkey, S. Das, S. Seal, J. Erlichman, K. Heckman, L. Ghibelli, E. Traversa, J. F. McGinnis, W. T. Self, *Environ. Sci.: Nano* **2015**, *2*, 33–53; b) T. Montini, M. Melchionna, M. Monai, P. Fornasiero, *Chem. Rev.* **2016**, *116*, 5987–6041; c) A. Dhall, W. Self, *Antioxidants* **2018**, *7*, 97; d) S.

Rajeshkumar, P. Naik, *Biotechnol. Rep.* **2018**, *17*, 1–5; e) N. Thakur, P. Manna, J. Das, *J. Nanobiotechnol.* **2019**, *17*, 84.
[6] a) H. Wu, F. Li, S. Wang, J. Lu, J. Li, Y. Du, X. Sun, X. Chen, J. Gao, D. Ling, *Biomaterials* **2018**, *151*, 66–77; b) H. A. Rather, R. Thakore, R. Singh, D. Jhala, S. Singh, R. Vasita, *Bioact. Mater.* **2018**, *3*, 201–211; c) M. Naseri-Nosar, S. Farzamfar, H. Sahrapeyama, S. Ghorbani, F. Bastami, A. Vaez, M. Salehi, *Mater. Sci. Eng. C* **2017**, *81*, 366–372; d) R. Davan, R. G. S. V. Prasad, V. S. Jakka, R. S. L. Aparna, A. R. Phani, B. Jacob, P. C. Salins, D. B. Raju, *J. Bionanosci.* **2012**, *6*, 78–83.
[7] a) D. V. Talapin, J.-S. Lee, M. V. Kovalenko, E. V. Shevchenko, *Chem. Rev.* **2010**, *110*, 389–458; b) J. J. Giner-Casares, M. Henriksen-Lacey, M. Corondao-Puchau, L. M. Liz-Marzán, *Mater. Today* **2016**, *19*, 19–28.
[8] T. S. Rodrigues, A. G. M. da Silva, P. H. C. Camargo, *J. Mater. Chem. A* **2019**, *7*, 5857–5874.
[9] N. T. K. Thanh, N. Maclean, S. Mahiddine, *Chem. Rev.* **2014**, *114*, 7610–7630.
[10] a) Y. Wang, J. He, C. Liu, W. H. Chong, H. Chen, *Angew. Chem. Int. Ed.* **2015**, *54*, 2022–2051; b) Y. Xia, X. Xia, H.-C. Peng, *J. Am. Chem. Soc.* **2015**, *137*, 7947–7966; c) Z. Wu, S. Yang, W. Wu, *Nanoscale* **2016**, *8*, 1237–1259.
[11] T. W. Hansen, A. T. Delariva, S. R. Challa, A. K. Datye, *Acc. Chem. Res.* **2013**, *46*, 1720–1730.
[12] C. T. Cambell, J. R. V. Sellers, *Faraday Discuss.* **2013**, *162*, 9–30.
[13] a) J. A. Farmer, C. T. Campbell, *Science* **2010**, *329*, 933–936; b) S. D. Senanayake, D. Stacchiola, J. A. Rodriguez, *Acc. Chem. Res.* **2013**, *46*, 1702–1711; c) S. Liu, L. Mei, X. Liang, L. Liao, G. Lv, S. Ma, S. Lu, A. Abdelkader, K. Xi, *ACS Appl. Mater. Interfaces* **2018**, *10*, 29467–29475; d) X. Tang, Y. Zeng, L. Cao, L. Yang, Z. Wang, D. Fang, Y. Gao, Z. Shao, B. Yi, *J. Mater. Chem. A* **2018**, *6*, 15074–15082; e) J. Zheng, M. Zhang, T. Miao, J. Yang, J. Xu, N. S. Alharbi, M. Wakeel, *Mater. Chem. Front.* **2019**, *3*, 224–232.
[14] Reviews: a) B. Zheng, X. Lin, X. Zhang, D. Wu, K. Matyjaszewski, *Adv. Funct. Mater.* **2019**, 1907006; b) N. Chaoui, M. Trunk, R. Dawson, J. Schmidt, A. Thomas, *Chem. Soc. Rev.* **2017**, *46*, 3302–3321; c) L. Tan, B. Tan, *Chem. Soc. Rev.* **2017**, *46*, 3322–3356; d) S. Das, P. Heasman, T. Ben, S. Qiu, *Chem. Rev.* **2017**, *117*, 1515–1563; e) Y. Xu, S. Jin, H. Xu, A. Nagai, D. Jiang, *Chem. Soc. Rev.* **2013**, *42*, 8012–8031; f) R. Dawson, A. I. Cooper, D. J. Adams, *Prog. Polym. Sci.* **2012**, *37*, 530–563; g) F. Vilela, K. Zhang, M. Antonietti, *Energy Environ. Sci.* **2012**, *5*, 7819–7832; h) D. Wu, F. Xu, B. Sun, R. Fu, H. He, K. Matyjaszewski, *Chem. Rev.* **2012**, *112*, 3959–4015.
[15] a) A. Patra, J.-M. Koenen, U. Scherf, *Chem. Commun.* **2011**, *47*, 9612–9614; b) K. Wu, J. Guo, C. Wang, *Chem. Commun.* **2014**, *50*, 695–697; c) B. C. Ma, S. Ghasimi, K. Landfester, F. Vilela, K. A. I. Zhang, *J. Mater. Chem. A* **2015**, *3*, 16064–16071; d) S. Bandyopadhyay, P. Pallavi, A. G. Anil, A. Patra, *Polym. Chem.* **2015**, *6*, 3775–3780; e) B. C. Ma, S. Ghasimi, K. Landfester, K. A. I. Zhang, *J. Mater. Chem. B* **2016**, *4*, 5112–5118; f) P. Pallavi, S. Bandyopadhyay, J. Louis, A. Deshmukh, A. Patra, *Chem. Commun.* **2017**, *53*, 1257–1260.
[16] a) D. H. Lee, K. C. Ko, J. H. Ko, S. Y. Kang, S. M. Lee, H. J. Kim, Y.-J. Ko, J. Y. Lee, S. U. Son, *ACS Macro Lett.* **2018**, *7*, 651–655; b) K. Cho, S. M. Lee, H. J. Kim, Y.-J. Ko, S. U. Son, *Chem. Commun.* **2019**, *55*, 3697–3700; c) D. W. Kim, D. H. Kim, J. Y. Jang, Y.-J. Ko, S. M. Lee, H. J. Kim, K. Na, S. U. Son, *J. Mater. Chem. B* **2019**, *7*, 4118–4123.
[17] S. Y. Kang, C. W. Kang, D. W. Kim, Y. Myung, J. Choi, S. M. Lee, H. J. Kim, Y.-J. Ko, S. U. Son, *Chem. Asian J.* **2019**, *14*, 3173–3180.
[18] a) J. Tan, J. Wan, J. Guo, C. Wang, *Chem. Commun.* **2015**, *51*, 17394–17397; b) L. Wang, W. Wang, X. Zheng, Z. Li, Z. Xie, *Chem. Eur. J.* **2017**, *23*, 1379–1385; c) X. Zheng, L. Wang, Q. Pei, S. He, S. Liu, Z. Xie, *Chem. Mater.* **2017**, *29*, 2374–2381; d) Z. Li, Y.-W. Yang, *J. Mater. Chem. B* **2017**, *5*, 9278–9290; e) J. Y. Jang, H. T. T. Duong, S. M. Lee, H. J. Kim, Y.-J. Ko, J. H. Jeong, D. S. Lee, T. Thambi, S. U. Son, *Chem. Commun.* **2018**, *54*, 3652–3655; f) J. Y. Jang, T. M. D. Le, J. H. Ko, Y.-J. Ko, S. M. Lee, H. J. Kim, J. H. Jeong, T. Thambi, D. S. Lee, S. U. Son, *Chem. Mater.* **2019**, *31*, 300–304.
[19] a) T. M. D. Le, H. T. T. Duong, T. Thambi, V. H. G. Phan, J. H. Jeong, D. S. Lee, *Biomacromolecules* **2018**, *19*, 3536–3548; b) M. H. Turabee, T. Thambi, D. S. Lee, *ACS Appl. Bio Mater.* **2019**, *2*, 2500–2510.
[20] S. Yuan, S. Kirklin, B. Dorney, D.-J. Liu, L. Yu, *Macromolecules* **2009**, *42*, 1554–1559.
[21] H. J. Kwon, D. Kim, K. Seo, Y. G. Kim, S. I. Han, T. Kang, M. Soh, T. Hyeon, *Angew. Chem. Int. Ed.* **2018**, *57*, 9408–9412.
[22] J.-X. Jiang, F. Su, A. Trewin, C. D. Wood, N. L. Campbell, H. Niu, C. Dickinson, A. Y. Ganin, M. J. Rosseinsky, Y. Z. Khimyak, A. I. Cooper, *Angew. Chem. Int. Ed.* **2007**, *46*, 8574–8578.
[23] a) T. Mokkelbost, I. Kaus, T. Grande, M.-A. Einarsrud, *Chem. Mater.* **2004**, *16*, 5489–5494; b) R. Zamiri, H. A. Ahangar, A. Kaushal, A. Zakaria, G. Zamiri, D. Tobaldi, J. M. F. Ferreira, *PLoS One* **2015**, *10*, e0122989.
[24] M. Longmire, P. L. Choyke, H. Kobayashi, *Nanomedicine* **2008**, *3*, 703–717.
[25] Y.-N. Zhang, W. Poon, A. J. Tavares, I. D. McGilvray, W. C. W. Chan, *J. Controlled Release* **2016**, *240*, 332–348.
[26] M. Jin, J.-N. Park, J. K. Shon, Z. Li, E. Lee, J. M. Kim, *J. Porous Mater.* **2013**, *20*, 989–995.
[27] H. Takeuchi, M. Ishida, A. Furuya, H. Todo, H. Urano, K. Sugibayashi, *Biol. Pharm. Bull.* **2012**, *35*, 192–202.
[28] B. Jachimska, A. Pajor, *Bioelectrochemistry* **2012**, *87*, 138–146.
[29] N. Kang, J. H. Park, M. Jin, N. Park, S. M. Lee, H. J. Kim, J. M. Kim, S. U. Son, *J. Am. Chem. Soc.* **2013**, *135*, 19115–19118.

Manuscript received: January 23, 2020
Revised manuscript received: April 4, 2020
Accepted manuscript online: April 6, 2020
Version of record online: ■■, ■■■

FULL PAPER

Microporous organic nanoparticle (MONP)@CeO_2 nanocomposites were engineered by the formation of CeO_2 materials in the presence of MONP. The amount of CeO_2 in the MONP@CeO_2 nanocomposites was optimized by the systematic control of Ce precursors. Compared to CeO_2 materials, the MONP@CeO_2 nanocomposites enhanced *in vivo* regenerative wound healing due to efficient scavenging of ROS and reduced cytotoxicity.

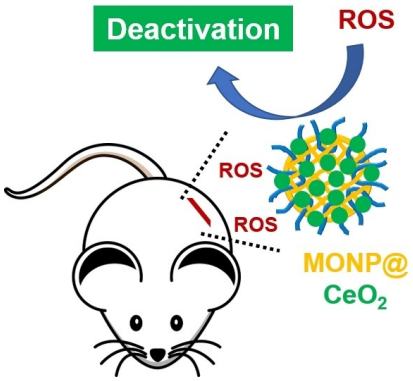

D. W. Kim, T. M. D. Le, Dr. S. M. Lee, Dr. H. J. Kim, Dr. Y.-J. Ko, Prof. J. H. Jeong, Dr. T. Thambi, Prof. D. S. Lee*, Prof. S. U. Son**